

Antibacterial and catalytic performance of rGO-CNT-ZrO₂ composite

Mizaj Shabil Sha, Surya Devarajan, Farzana N. Musthafa, Nahla O. Eltai, Swathi Ippili, Venkatraju Jella, Soon-Gil Yoon, Hamad Al-Lohedan, R Jothi Ramalingam & Kishor Kumar Sadasivuni

To cite this article: Mizaj Shabil Sha, Surya Devarajan, Farzana N. Musthafa, Nahla O. Eltai, Swathi Ippili, Venkatraju Jella, Soon-Gil Yoon, Hamad Al-Lohedan, R Jothi Ramalingam & Kishor Kumar Sadasivuni (03 Jul 2023): Antibacterial and catalytic performance of rGO-CNT-ZrO₂ composite, International Journal of Environmental Analytical Chemistry, DOI: [10.1080/03067319.2023.2230146](https://doi.org/10.1080/03067319.2023.2230146)

To link to this article: <https://doi.org/10.1080/03067319.2023.2230146>



© 2023 The Author(s). Published by Informa UK Limited, trading as Taylor & Francis Group.



Published online: 03 Jul 2023.



Submit your article to this journal [↗](#)



Article views: 789



View related articles [↗](#)



View Crossmark data [↗](#)



Citing articles: 1 View citing articles [↗](#)

Antibacterial and catalytic performance of rGO-CNT-ZrO₂ composite

Mizaj Shabil Sha^a, Surya Devarajan^a, Farzana N. Musthafa^a, Nahla O. Eltai^b, Swathi Ippili^c, Venkatraju Jella^c, Soon-Gil Yoon^c, Hamad Al-Lohedan^d, R Jothi Ramalingam^d and Kishor Kumar Sadasivuni^a

^aCenter for Advanced Materials, Qatar University, Doha, Qatar; ^bBiomedical Research Center, Qatar University, Doha, Qatar; ^cDepartment of Materials Science and Engineering, Chungnam National University, Daejeon, Republic of Korea; ^dChemistry Department, College of Science, King Saud University, Riyadh, Kingdom of Saudi Arabia

ABSTRACT

In recent years, there has been a rise in public awareness regarding antibacterial properties and commercial opportunities for their use in the medical field. The current study describes the fabrication of a ternary composite, reduced graphene oxide-carbon nanotubes-zirconium oxide (rGO-CNT-ZrO₂), and their potential applications for antimicrobial activity and catalytic degradation of neutral red, indigo carmine and eriochrome black-T dyes. In addition, the capability of nanocomposite for UV sensing was examined. These nanocomposites were made using the hydrothermal method. TEM, SEM, FTIR, TGA and XRD were used to characterise and investigate the properties of nanocomposite, and the disc diffusion technique was used to assess their antimicrobial activity. These findings suggest that the developed composite has excellent antimicrobial properties, which could be helpful in the pharmaceutical and medical industries.

ARTICLE HISTORY

Received 25 January 2023
Accepted 10 May 2023


KEYWORDS

Antimicrobial; dye degradation; reduced graphene oxide; carbon nanotubes; zirconium oxide

1. Introduction

As part of the global effort to reduce the risks of infectious bacteria and epidemic outbreaks to human health, antibacterial composites are receiving increased attention in research and development. As a result, incorporating antibacterial substances into life is critical in some applications where bacteria spread must be limited in contaminated environments [1,2]. Medical and surgical clothing, mattress covers, curtains, bedding, and wipes are all included in this aspect. The biological environment significantly impacts metal oxides' antibacterial properties [3,4]. The nanocomposites' size, stability, and concentration (NCs) are the primary driving forces behind their bacterial activity [5,6].

Organic dye molecules, widely used in industries such as textiles, paints, paper, cosmetics, and plastics, are among the most serious threats to human health and aquatic life in the developing world [7]. Neutral red (NR) is commonly used as a histological stain for lysozymes. Still, it has also been used in virus research as a pH indicator, DNA

CONTACT Kishor Kumar Sadasivuni  kishor_kumars@yahoo.com

© 2023 The Author(s). Published by Informa UK Limited, trading as Taylor & Francis Group.

This is an Open Access article distributed under the terms of the Creative Commons Attribution License (<http://creativecommons.org/licenses/by/4.0/>), which permits unrestricted use, distribution, and reproduction in any medium, provided the original work is properly cited. The terms on which this article has been published allow the posting of the Accepted Manuscript in a repository by the author(s) or with their consent.

determination using optical and electrochemical methods, and evaluation of synthetic and naturally derived biomaterials [8]. Indigo carmine (IC) is a food colouring, a histological dye and a two-colour indicator. An anionic azo dye, eriochrome black T (EBT), is commonly used in industrial applications such as dyeing, laser printing, and painting [9–11]. The excessive use of these dyes pollutes the environment and is toxic [12,13]. Removing this dye from water is critical for humans and aquatic life [14]. Nanocatalyst-based dye degradation has gained popularity due to nanoparticles' increased surface-volume ratio, long shelf life, and enhanced catalytic activity [15,16].

Despite graphene's outstanding properties, its use in textile modification is limited by the difficulty of obtaining stable aqueous dispersions applicable to natural hydrophilic fibres. Graphene oxide (GO) functional groups facilitate dispersal in water but impair electrical conductivity, so GO must be reduced chemically or thermally to rGO [17]. Carbon nanomaterials have outstanding optical, thermal, mechanical, and antibacterial properties, making them ideal in the biomedical and food industry. Despite this, their practical applications as antimicrobial agents have yet to be fully explored due to their relatively poor dispersibility, cost, and scalability changes [18]. rGO and CNT are already explored for dye degradation [19,20].

ZrO₂ has been widely used because of its cost-effectiveness, physical and chemical stability, and superior photocatalytic activities for UV radiation excitation via absorption, scattering, and light reflection [21]. ZrO₂ has a large band gap in the 5–7 eV range, limiting its visible photocatalytic activity [22]. Several strategies for closing the band gap have been developed, including coupling with metal oxides and metallic and non-metallic elements. The band gap has not been reduced by metal or non-metal doping alone [23].

On the other hand, metal doping has exhibited excellent photocatalytic activity results. Metal doping causes thermal instability and increases carrier-recombination centres [24]. Metal oxides have been doped into non-metal elements like carbon, nitrogen, phosphorus, sulphur, fluorine, and bismuth to increase photocatalytic activity. Carbon and sulphur are highly oxidising elements with ionic radiuses at 170 and 180 pm, respectively. These values are more significant than oxygen (152 pm), allowing the non-metal ions to replace one another or occupy an interstitial position in ZrO₂. Furthermore, in ZrO₂, the 2p and 3p states of carbon are combined with the oxygen of the 2p state, and effective band gap narrowing occurs. During chemical bonding, carbon can also form in C⁴⁺ [25].

Much research has been conducted using rGO-CNT composites [26–32]. Most of them have found applications in sensing or electronics-related applications. Herein we have fabricated an rGO-CNT-ZrO₂ composite, which has applications in different areas. rGO-CNT-ZrO₂ catalyst is a composite material consisting of reduced graphene oxide (rGO), carbon nanotubes (CNTs), and zirconia (ZrO₂) nanoparticles. Due to its unique properties, this composite material has been widely studied as a catalyst in various chemical reactions. The rGO-CNT-ZrO₂ nanocomposite can serve as a highly effective catalyst due to the unique properties of its components. Reduced graphene oxide (rGO) is a form of graphene, a single layer of carbon atoms arranged in a hexagonal lattice structure. rGO possesses high electrical conductivity and a large surface area, which can promote the adsorption of NR molecules and facilitate electron transfer reactions during the degradation process. Carbon nanotubes (CNTs) are cylindrical nanostructures made of carbon atoms with exceptional mechanical and electrical properties. CNTs can act as nanoscale conduits for electron transfer, enhancing the catalytic activity of the composite. Zirconium

oxide (ZrO_2) is a metal oxide with high thermal stability and excellent catalytic properties. Here are some advantages and disadvantages of the rGO-CNT- ZrO_2 catalyst:

Advantages:

- High catalytic activity: The rGO-CNT- ZrO_2 catalyst has a high surface area, providing many active sites for the reaction. This leads to higher catalytic activity compared to other catalysts.
- Stability: The presence of rGO and CNTs makes the catalyst more stable, which helps maintain the catalytic activity over a longer period.
- Reusability: The rGO-CNT- ZrO_2 catalyst can be easily separated from the reaction mixture and reused multiple times, making it a cost-effective option.
- Selectivity: The catalyst has high selectivity towards specific products in certain reactions, which is important in industries where specific products are desired.

Disadvantages:

- Synthesis complexity: The synthesis of the rGO-CNT- ZrO_2 catalyst is complex and requires expertise and equipment, making it difficult to scale up the production.
- Cost: The raw materials used in synthesising the catalyst, such as CNTs and zirconia nanoparticles, is relatively high, which may make the catalyst expensive.

The rGO-CNT- ZrO_2 nanocomposite can exhibit excellent UV sensing capabilities due to its individual components' synergistic effects. When used as a UV sensor, the rGO-CNT- ZrO_2 nanocomposite typically acts as a photoactive material that can generate measurable electrical signals in response to UV radiation. The exact mechanism of UV sensing by rGO-CNT- ZrO_2 can vary depending on the nanocomposite composition and device configuration.

In this study, we looked at the catalytic activity of rGO-CNT- ZrO_2 NCs on the degradation of NR, IC and EBT. In addition, the antimicrobial activity of NCs was investigated. These findings indicate that the composite has promising antibacterial and catalytic performance.

2. Materials and methods

2.1. Chemicals

Carbon nanotubes (CNTs), graphite flakes, neutral red (NR), indigo carmine (IC), eriochrome black T, sulphuric acid (H_2SO_4 , 95.0–98.0%), phosphoric acid (H_3PO_4 , 85.0%), nitric acid (HNO_3 , 65%), ethanol and ammonia were supplied by E-Merck(Germany). Zirconyl nitrate hydrate ($\text{ZrO}(\text{NO}_3)_2 \cdot \text{H}_2\text{O}$) was purchased from Sigma Aldrich. The solution was made with locally sourced deionised water (DI). All of the abovementioned analytical reagent-grade chemicals were used without further purification.

2.2. Methods

2.2.1. Synthesis of graphene oxide

The graphene oxide (GO) starting material was created by chemically oxidising graphite flakes in H_2SO_4 and H_3PO_4 . The GO sample was dried for three days in a vacuum oven at 45 °C before being dispersed in DI water using a bath sonicator.

2.2.2. Purification of MWCNTs

Commercial MWCNTs were purified for 24 hours and soaked in a 70% nitric acid solution at 90 °C (specific surface area: 5–20 µm length: 40–300 cm² g⁻¹). Following the reaction, the mixture was filtered through a 0.2 mm nylon membrane filter and washed with excess DI water until the pH was neutral. Before further use, the purified and functionalised MWCNTs were dried for 12 hours in a 100 °C oven.

2.2.3. Synthesis of rGO-CNT- ZrO₂ nanocomposites

rGO-CNT-ZrO₂ nanocomposites were synthesised using the well-known hydrothermal method. Purified carbon nanotubes were ultrasonically dispersed in 40 mL of GO dispersions. In this study, the GO/CNTs ratio was kept constant (10: 1), and 150 mg Zirconyl nitrate hydrate (ZrO(NO₃)₂.H₂O) was mixed into 40 mL of GO/CNTs dispersions and stirred for 1 hour before adding urea and stirring for another hour. This mixture's pH was changed to 10 with an ammonia solution before being transferred to a sealed autoclave. For 8 hours, the reaction temperature was kept at 180 °C. After the hydrothermal reaction, the material was filtered and washed with excess water and ethanol several times.

2.2.4. Characterization of metal oxides

The XRD pattern was acquired using a Cu target on a Malvern Panalytical Xpert X-Ray diffractometer (45 kV, 40 mA). After dispersing the materials in ethanol, they were loaded onto a copper grid for transmission electron microscopy (TEM) with an FEI Tecnai G2 S-Twin FEG 200kV TEM. The powder was dispersed in isopropanol using a bath sonicator for 10–20 minutes before being drop casted on carbon film 200 copper mesh and air-dried before analysis. The purity of nanopowder was determined using a Thermo Nicolet Nexus 670 FTIR spectrometer. Thermogravimetric analysis was carried out using Perkin-Elmer thermogravimetric analyser TGA 4000.

2.2.5. Antibacterial activity analysis- Disc diffusion method

The disk diffusion method is one of the most adaptable antimicrobial susceptibility testing methods. The technique involves seeding a lawn of bacteria on the surface of an agar medium with antimicrobial-saturated paper disks, incubating the plate overnight, and measuring the presence or absence of an inhibition zone around the disks. The blank disk, 6 mm in diameter (Liofilchem®, Roseto Degli Abruzzi, Italy), was immersed in the nanocomposite for 5 minutes. The disk was then lawned with *Escherichia coli* bacteria (*E. coli* bacteria) suspension adjusted to 0.5 McFarland standard as measured by DensiCHEK Plus (bioMérieux, Marcy l'Etoile, France) using sterile forceps and placed on a nutrient agar (Himedia, Mumbai, India) plate. The mixture was then incubated at 37 °C for 6–24 hours. To determine the antibacterial effect, the zone of inhibition was measured.

2.2.6. Dye degradation analysis

15 mg of the photocatalyst was measured and added to 20 mL of distilled water. The solution was then sonicated for about 30 minutes for a uniform suspension. Approximately 5 mL is added to aqueous solutions of NR, EBT and IC [40 mL]. Afterwards, the sample solution was kept in the dark for about 30 minutes, allowing the reaction to reach adsorption equilibrium. After 30 minutes of keeping it in darkness, 3 mL of the sample is withdrawn and analysed using UV-vis spectroscopy. The solution was

held under the sunlight with constant magnetic stirring. During this time, aliquots of supernatant solution were withdrawn at intervals of 20 minutes until 3 hours and subjected to UV-vis analysis. The absorbance vs wavelength plots were drawn. From the plot, adsorption percentage and photodegradation efficiency were calculated.

2.2.7. UV sensing

A sample for analysis was prepared by making a composite slurry with ethanol. 2 μL of the slurry was coated on an interdigital electrode (IDE) of 5 μm slide using a micropipette and placed in a box. This apparatus was connected to a hantek for measurements (Figure 1). Initially, for 30 seconds, the UV light kept at a distance of 5 cm (365 nm, 0.6 mW/cm^2) was turned off, followed by keeping it on and off for 30 seconds for the next five minutes. Data was collected and analysed.

3. Results and discussion

3.1. Characterization

The XRD patterns for rGO, CNT, ZrO_2 , and rGO-CNT- ZrO_2 nanocomposites are shown in Figure 2(a). The diffraction peak for rGO is identified at $2\theta = 24.57^\circ$ with a d-spacing of 3.62 nm. The ternary nanocomposites rGO-CNT- ZrO_2 of face-centre cubic ZrO_2 , respectively (JCPDS 78-0694). According to Debye-Scherrer's equation, the average crystalline size of cerium nanocrystals in rGO-CNT- ZrO_2 was 11.5 nm. Diffraction peaks of rGO and MWCNT were not observed in the rGO-CNT- ZrO_2 ternary nanocomposite due to the low degree of graphitisation generated by the deposition of ZrO_2 nanoparticles on their surfaces.

The surface functional groups were revealed using FTIR measurements (Figure 2(c)). Functionalised CNTs had characteristic peaks at 2925 cm^{-1} (C-H asymmetric stretching), 2854 cm^{-1} (C-H symmetric stretching), 3410 cm^{-1} (O-H stretching), 1603 cm^{-1} (C=O stretching), 1420 cm^{-1} (C=C stretching), 1265 cm^{-1} (O-H bending vibration), and 1080 cm^{-1}

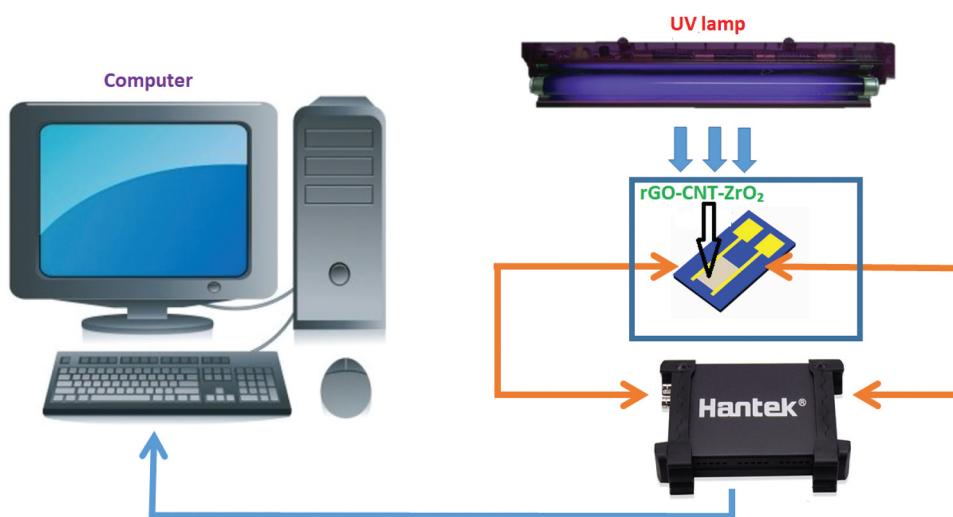


Figure 1. Experimental setup for UV sensing.

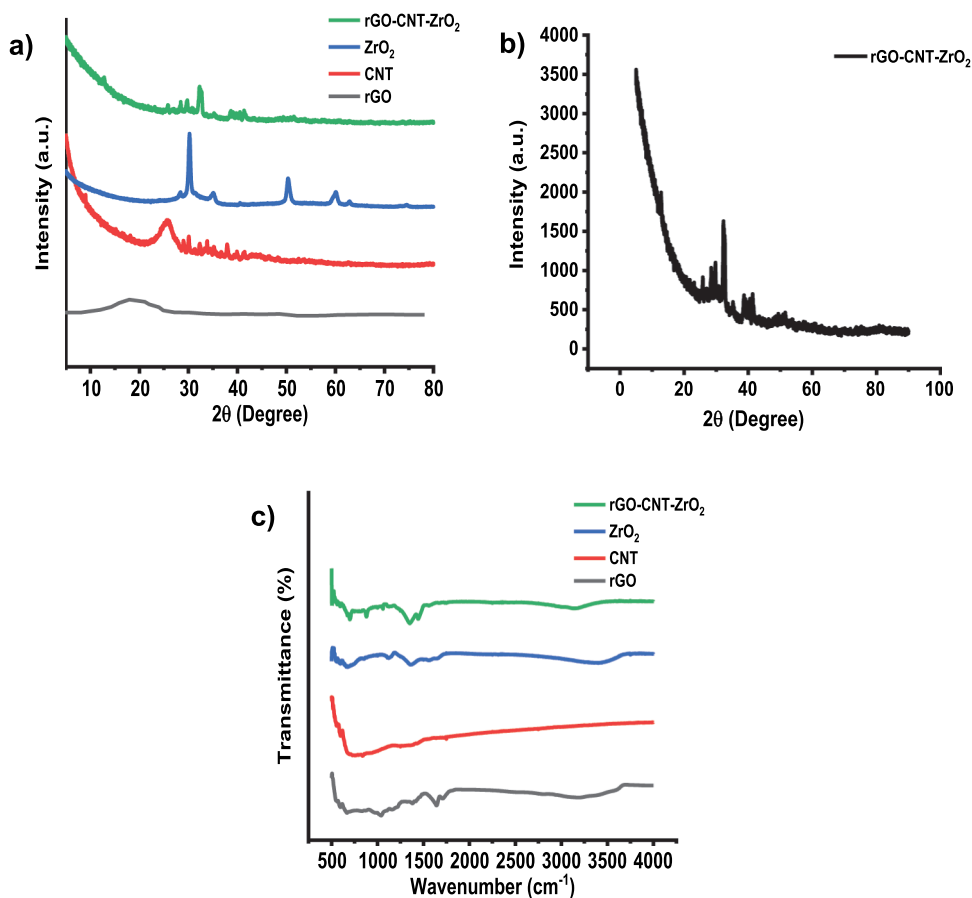


Figure 2. XRD patterns (a) before dye degradation (b) after dye degradation (c) FTIR spectra of rGO, CNT, ZrO₂, and rGO-CNT-ZrO₂.

(C-O stretching vibration). This discovery supports the formation of ZrO₂ nanoparticles on the surface of CNTs. In the rGO-CNT-ZrO₂ ternary nanocomposite, the skeletal vibration of C=C at 1558 cm⁻¹ and C-O-C stretching at 1054 cm⁻¹ of rGO and Zr-O stretching at 490 cm⁻¹ were observed, while the carbonyl group (1724 cm⁻¹) was absent. These results demonstrate the formation of ZrO₂ nanoparticles and confirm the conversion of GO to rGO during in situ reductions of the rGO-CNT-ZrO₂ ternary nanocomposite [33].

Figure 3 shows TEM and SEM images of the ternary nanocomposite rGO-CNT-ZrO₂. In the rGO-CNT-ZrO₂ nanocomposite, ZrO₂ nanoparticles were found to be uniformly distributed on rGO-CNT surfaces (Figure 3(a,b)). The morphology of the prepared RGO-CNT-ZrO₂ nanocomposites was also examined using FE-SEM (Figure 3(c)). CNTs in the RGO-CNT-ZrO₂ nanocomposites were visible in the images depicted as a red circle. It is assumed that including CNTs (0.83 nm) in the above composites slows the restacking rate of graphene sheets while facilitating uniform ZrO₂ formation on the graphene surface.

Figure 4 displays the TGA patterns for rGO, CNT, ZrO₂ and rGO-CNT-ZrO₂ nanocomposite. It was observed that The TGA curve of rGO exhibited an overall weight loss of 30% within the experimental temperature range due to the

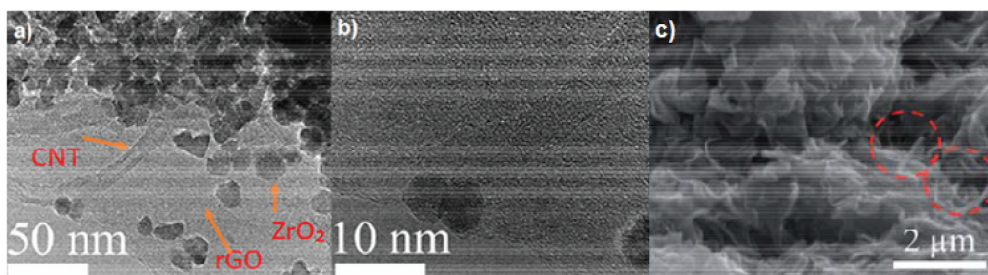


Figure 3. (a) TEM and (b) HRTEM (c) SEM images of the rGO-CNT-ZrO₂ ternary nanocomposite.

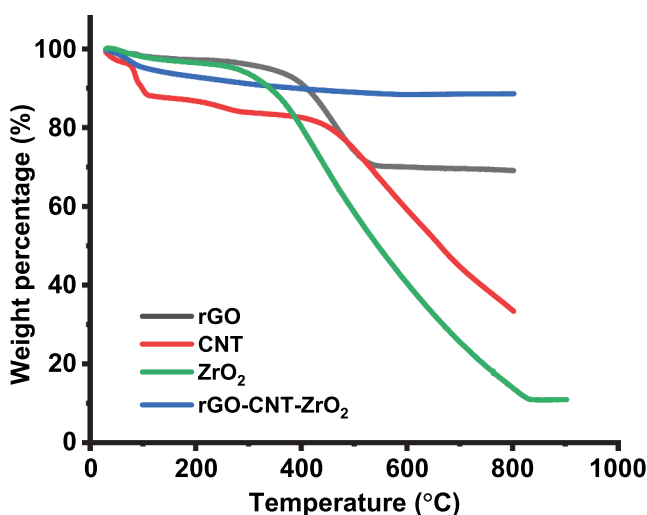


Figure 4. TGA curves of rGO, CNT, ZrO₂ and rGO-CNT-ZrO₂ ternary nanocomposite.

reduction of the oxygen-containing functional groups. CNT had a weight loss of 65%, whereas ZrO₂ had a loss of 90%. The composite displayed a total weight loss of 10% in the identical temperature range.

3.2. Antibacterial properties

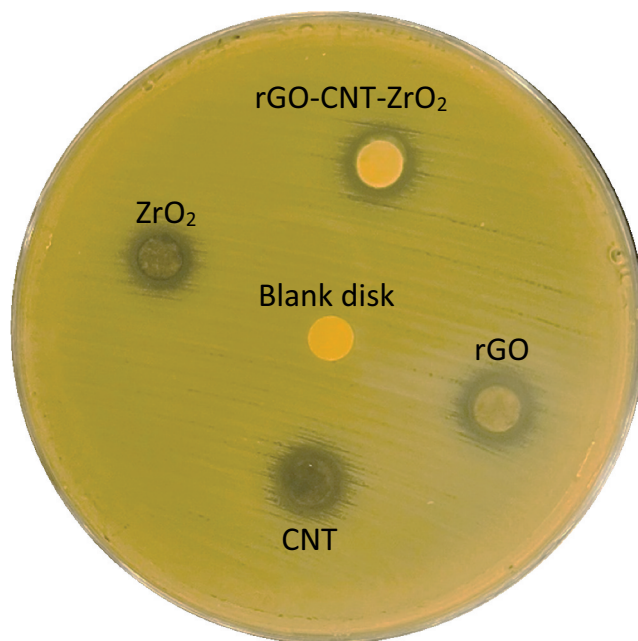
The diameter of the inhibition zone around the discs was measured to assess antibacterial activity. The test was repeated three times. The antibacterial activity of the composite was expressed as the mean zone of inhibition diameters (mm). Antibacterial activity was checked for individual components also (Table 1). The composite was highly effective in antibacterial properties (Figure 5).

3.3. Dye degradation

The prepared catalyst and its components were analysed for dye degradation, and it was observed that rGO-CNT-ZrO₂ could degrade three dyes: NR, IC and EBT (Table 2). Figure 6 illustrates the photocatalytic activity of different rGO in NR, EBT and IC.

Table 1. Antibacterial activity of components against *E. coli* bacteria as demonstrated by the inhibition zone.

Materials	Zone of inhibition (mm) against <i>E. coli</i> bacteria										Mean diameter (mm)
	Trial 1	Trial 2	Trial 3	Trial 4	Trial 5	Trial 6	Trial 7	Trial 8	Trial 9	Trial 10	
rGO-CNT-ZrO ₂	10	8	12	12	8	10	9	8	11	12	10
rGO	2	1	0	0	1	1	0	2	1	2	1
CNT	0	0	0	0	0	0	0	0	0	0	0
ZrO ₂	0	0	0	0	0	0	0	0	0	0	0

**Figure 5.** Disc diffusion test for the antibacterial effect of the materials.**Table 2.** Dye degradation analysis by composite.

Material	Dyes degraded		
rGO	Neutral red	-	Eriochrome black T
CNT	Neutral red	-	-
ZrO ₂	-	-	Eriochrome black T
rGO-CNT-ZrO ₂	Neutral red	Indigo carmine	Eriochrome black T

Figure 7 depicts the possible degradation pathway for EBT dye, which concluded that OH free radicals attacked the azo group present in EBT dye, resulting in unstable intermediates identified as 2-Nitronaphthalene and naphthalene-1-ol. The NO₂ group is a strong electron-withdrawing, whereas the azo group is electron-donating. OH free radicals are more likely to attack the azo group than the nitro group because an attack on the azo group allows them to balance their unpaired electronic configuration by directly adding themselves. Furthermore, the N-C bond of the nitro group is more stable than the N-C bond of

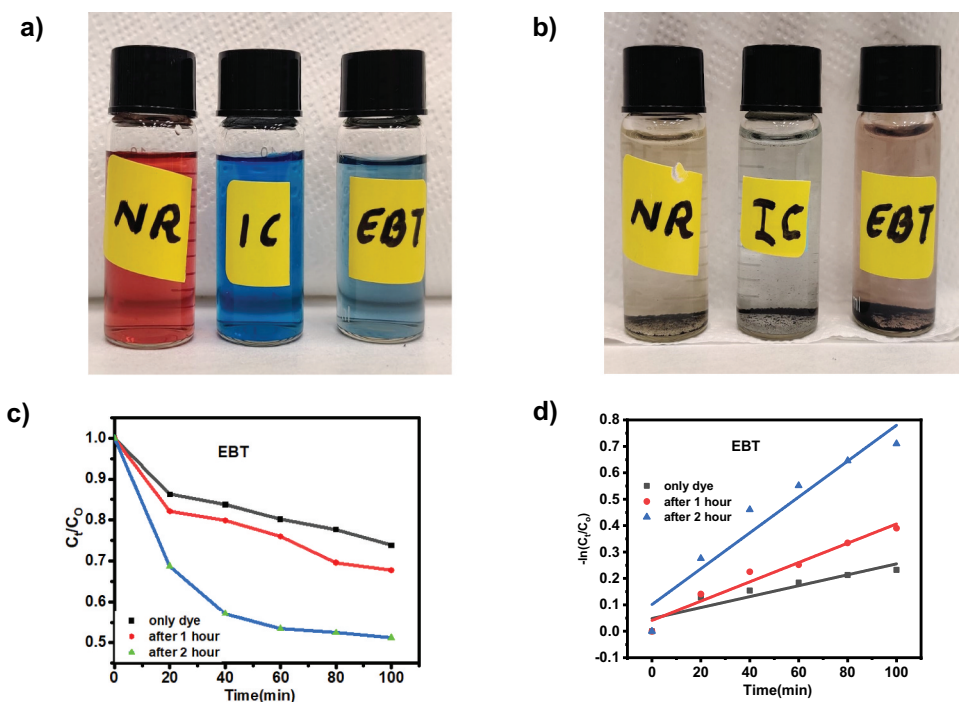


Figure 6. Dye degradation analysis of rGO-CNT-ZrO₂ in different dyes. (a) before adding nanocomposite, (b) degraded dyes after adding nanocomposite, (c) degradation of EBT dye normalized against adsorption, and (d) pseudo-first-order kinetic plot of EBT dyes, respectively.

the azo group due to the resonance effect, which the azo group does not have. NR and IC degradation by rGO-CNT-ZrO₂ can occur through various mechanisms, including adsorption, oxidation, and reduction. The rGO-CNT-ZrO₂ nanocomposite can adsorb NR and IC molecules onto its surface through van der Waals forces, π - π , and electrostatic interactions. Once adsorbed, the molecules can undergo oxidation or reduction reactions facilitated by the catalytic properties of rGO, CNTs, and ZrO₂, leading to the degradation of dyes into smaller, less toxic compounds. The high surface area and electrical conductivity of rGO and CNTs, combined with the catalytic properties of ZrO₂, provide synergistic effects that can significantly enhance the degradation efficiency of dyes.

Using the following equations, the adsorption percentage (% C_{ads}) and photodegradation efficiency (% C_{deg}) was calculated:

$$\% C_{ads} = [(C_{initial} - C_0)/C_{initial}] * 100\% \quad (1)$$

$$\% C_{deg} = [(C_0 - C_t)/C_0] * 100\%, 0 \leq t \leq 3\text{hrs} \quad (2)$$

$C_{initial}$, C_0 , and C_t are the dye concentrations at the beginning, after reaching adsorption-desorption equilibrium, and at time t . The photocatalytic degradation reaction was then modelled using the pseudo-zero, first and second order kinetic equations depicted below:

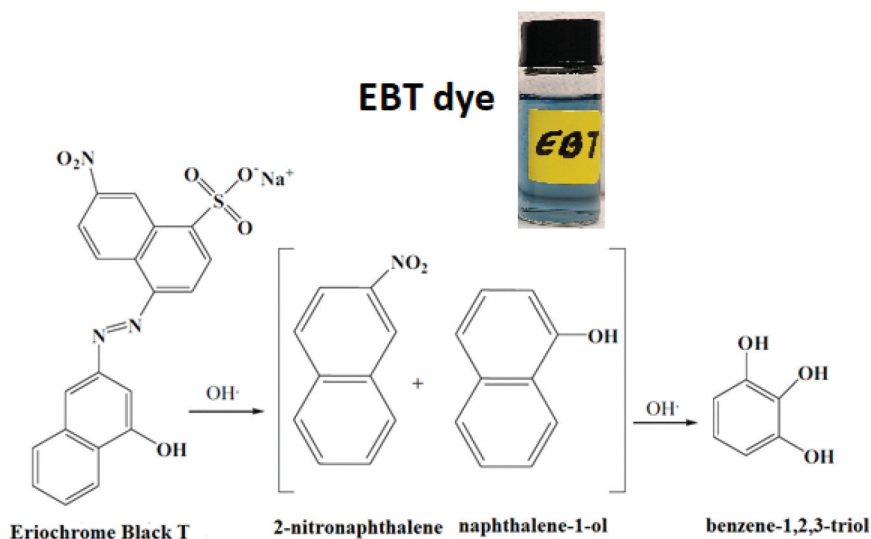


Figure 7. Predicted photodegradation mechanism of EBT.

$$C_t = C_0 - k_0 t \quad (3)$$

$$C_t = C_0 e^{-k_1 t} \quad (4)$$

$$d[C]/dt = k_2 [C]^2 \quad (5)$$

k_0 ($\text{mg L}^{-1} \text{min}^{-1}$), k_1 (min^{-1}) and k_2 ($\text{L mg}^{-1} \text{min}^{-1}$) denotes the pseudo-zero, first and second order rate constant. Table 3 displays the percentages of C_{ads} , C_{deg} , k , and R^2 . The results indicated that the dye degradation kinetics followed the first-order kinetics well.

After the degradation of the dyes using rGO-CNT-ZrO₂, the catalyst was regenerated from the degraded dyes by filtration. After filtration, The catalyst was thoroughly washed and cleaned to remove any residual dye or reaction byproducts that may have accumulated on its surface during degradation. This was done using ethanol and water, then drying to remove excess moisture. Figure 2(b) represents the XRD of the regenerated catalyst. No additional peaks were observed compared to Figure 2(a), indicating greater stability of the composite.

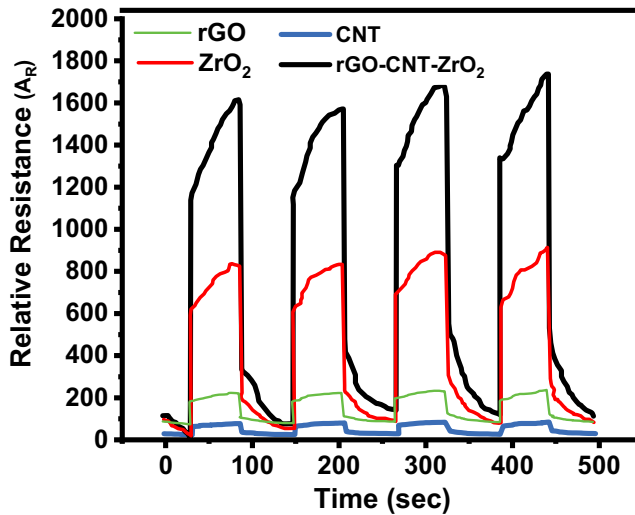
3.4. Photo sensing

Figure 8 shows the photosensitivity characteristics of the nanocomposite as a function of time (with and without UV illumination). Photosensitivity increases when UV light is used to illuminate and decreases when the UV light is turned off. UV sensors based on rGO-CNT-ZrO₂ have high photosensitivity compared to individual elements.

The UV detection mechanism is as follows: oxygen molecules are absorbed by trapping electrons on the surface of the nanocomposite when exposed to UV light. as shown by

Table 3. Dye adsorption percentage, photocatalytic degradation efficiency, and photocatalytic degradation rate.

Dyes	Adsorption percentage (%)	Photocatalytic degradation efficiency	k			R ²		
			k ₀	k ₁	k ₂	Zero order	First order	Second order
Eriochrome black T	10.3	8.23	0.00489	0.00526	0.00514	0.89	0.956	0.932
Neutral red	12.4	11.91	0.00521	0.00553	0.00539	0.927	0.97	0.91
Indico carmine	20.53	15.83	0.00571	0.00596	0.00534	0.953	0.999	0.91

**Figure 8.** UV sensing characteristics of Rgo-CNT-ZrO2.

This results in a decrease in carrier concentration and the formation of a depletion layer, which directly impacts the decreasing conductance. When exposed to UV light, electron-hole pairs are formed (Equation (5))



As shown by Equation (6), the overall reaction will be



The holes will rise to the surface and capture adsorbed oxygen ions, decreasing the depletion layer. The unpaired electrons in the conduction channel will move independently along the current stream. After the UV light is turned off, the electron-hole pairs will be recaptured.

4. Conclusion

In conclusion, we used a hydrothermal approach to create a high-quality rGO-CNT-ZrO₂ nanocomposite powder sample. The XRD and TEM analyses show the cubic

phase of ZrO₂ nanoparticles. Prepared composites exhibit outstanding antibacterial activity along with other catalytic properties. The prepared catalysts were tested for visible light degradation of different dyes, indicating higher photocatalytic activity of rGO-CNT-ZrO₂. Studies on photocatalytic activity revealed that rGO in composite improves adsorption in the dark and the photodegradation efficiency of nanocomposites when exposed to visible light. And the composite has the highest photocatalytic activity against NR, IC and EBT dye of any of the catalysts tested. Furthermore, a UV-sensor devices was developed based on the nanocomposite and it demonstrated high photosensitivity, and fast response

Acknowledgments

This work was supported by the Qatar University internal grant QPH3P-CAM-2021-452. The statements made herein are solely the responsibility of the authors. Open Access funding provided by the Qatar National Library. The author Jothi Ramalingam, acknowledge the financial support through Researchers Supporting Project number (RSP2023R354), King Saud University, Riyadh 11451, Saudi Arabia.

Disclosure statement

No potential conflict of interest was reported by the author(s).

Funding

This work was supported by Qatar university under the Grant no. QPH3P-CAM-2021-452 and Researchers Supporting Project number (RSP2023R54), King Saud university, Saudi Arabia. The statements made herein are solely the responsibility of the authors

References

- [1] B. Balasubramaniam, S. Prateek Ranjan, M. Kar, P. Saraf, S.P. Singh, V.K. Thakur, A. Gupta and R. K. Singh, *ACS Pharmacol. Transl. Sci.* **4** (1), 8–54 (2020). doi:10.1021/acsptsci.0c00174.
- [2] R. Khoshbakht, M. Kabiri, A. Neshani, M.N. Khaksari, S.M. Sadrzadeh, S.M. Mousavi, K. Ghazvini and M. Ghavidel, *Antimicrob. Resist. Infect. Control* **11** (1), 121 (2022). doi:10.1186/s13756-022-01159-y.
- [3] X. Song, L. Vossebein and A. Zille, *Antimicrob. Resist. Infect. Control* **8** (1), 139 (2019). doi:10.1186/s13756-019-0595-2.
- [4] U. Anand, M. Carpena, M. Kowalska-Górska, P. Garcia-Perez, K. Sunita, E. Bontempi, A. Dey, M.A. Prieto, J. Proćków and J. Simal-Gandara, *Sci. Total Environ.* **821**, 153472 (2022). doi:10.1016/j.scitotenv.2022.153472.
- [5] S.A. Rajan, A. Khan, S. Asrar, H. Raza, R.K. Das and N.K. Sahu, *IET Nanobiotechnol.* **13** (7), 682–687 (2019). doi:10.1049/iet-nbt.2018.5330.
- [6] K. Ivanova, A. Ivanova, E. Ramon, J. Hoyo, S. Sanchez-Gomez and T. Tzanov, *ACS Appl. Mater. Interfaces* **12** (32), 35918–35927 (2020). doi:10.1021/acsami.0c09364.
- [7] A.M. Elgarahy, K.Z. Elwakeel, S.H. Mohammad and G.A. Elshoubaky, *Cleaner Eng. Technol.* **4**, 100209 (2021). doi:10.1016/j.clet.2021.100209.
- [8] A. Steinegger, O.S. Wolfbeis and S.M. Borisov, *Chem. Rev.* **120** (22), 12357–12489 (2020). doi:10.1021/acs.chemrev.0c00451.
- [9] L. Dubenska and G.D. Levitskaya, *J. Anal. Chem.* **54**, 655–657 (1999).

- [10] E. Rápó, K. Posta, A. Csavdári, B.É. Vincze, G. Mara, G. Kovács, I. Haddidi and S. Tonk, *Crystals* **10** (7), 565 (2020). doi:10.3390/cryst10070565.
- [11] M. Zubair, N. Jarrah, M. Manzar, M. Al-Harathi, M. Daud, N. Mu'azu and S. Haladu, *J. Mol. Liq.* **230**, 344–352 (2017). doi:10.1016/j.molliq.2017.01.031.
- [12] R. Al-Tohamy, S.S. Ali, F. Li, K.M. Okasha, Y.A.-G. Mahmoud, T. Elsamahy, H. Jiao, Y. Fu and J. Sun, *Ecotoxicol. Environ. Saf.* **231**, 113160 (2022). doi:10.1016/j.ecoenv.2021.113160.
- [13] A. Roy, A. Sharma, S. Yadav, L.T. Jule and R. Krishnaraj, *Bioinorg. Chem. Appl.* **2021**, 1764647 (2021). doi:10.1155/2021/1764647.
- [14] O. Tavakoli, V. Goodarzi, M.R. Saeb, N.M. Mahmoodi and R. Borja, *J. Hazard. Mater.* **334**, 256–266 (2017). doi:10.1016/j.jhazmat.2017.04.023.
- [15] M. Batool, W.M. Daoush and M.K. Hussain, *Crystals* **12** (5), 662 (2022). doi:10.3390/cryst12050662.
- [16] A.K.D. Alsukaibi, *Processes* **10** (10), 1968 (2022). doi:10.3390/pr10101968.
- [17] J. Molina, *RSC Adv.* **6** (72), 68261–68291 (2016). doi:10.1039/C6RA12365A.
- [18] A.M. Díez-Pascual, *Int. J. Mol. Sci.* **22**, 10511 (2021). doi:10.3390/ijms221910511.
- [19] H. Khojasteh, M. Salavati-Niasari and F.S. Sangsefidi, *J. Alloys Compd.* **746**, 611–618 (2018). doi:10.1016/j.jallcom.2018.02.345.
- [20] N.P. Rajkumari, S. Dolakashoria and P. Goswami, *ACS Omega* **6** (4), 2686–2698 (2021). doi:10.1021/acsomega.0c04889.
- [21] J.O. Tijani, E.I. Odeh, S. Mustapha, T.C. Egbosiuba, A.I. Daniel, A.S. Abdulkareem and F.N. Muya, *Cleaner Chem. Eng.* **3**, 100034 (2022). doi:10.1016/j.clce.2022.100034.
- [22] G. Tian, K. Pan, H. Fu, L. Jing and W. Zhou, *J. Hazard. Mater.* **166** (2–3), 939–944 (2009). doi:10.1016/j.jhazmat.2008.11.090.
- [23] E. Vijayakumar, M. Govinda Raj, M.G. Narendran, R. Preetha, R. Mohankumar, B. Neppolian and A. John Bosco, *ACS Omega* **7** (6), 5079–5095 (2022). doi:10.1021/acsomega.1c06089.
- [24] M.L. Matias, A. Pimentel, A.S. Reis-Machado, J. Rodrigues, J. Deuermeier, E. Fortunato, R. Martins and D. Nunes, *Nanomaterials (Basel)* **12** (6), 1005 (2022). doi:10.3390/nano12061005.
- [25] P. Akhter, A. Arshad, A. Saleem and M. Hussain, *Catalysts* **12** (11), 1331 (2022). doi:10.3390/catal12111331.
- [26] F. Yin, Y. Guo, H. Li, W. Yue, C. Zhang, D. Chen, W. Geng, Y. Li, S. Gao and G. Shen, *Nano. Res.* **15** (10), 9341–9351 (2022). doi:10.1007/s12274-022-4440-1.
- [27] S.H. Kang, G.Y. Lee, J. Lim and S.O. Kim, *ACS Omega* **6** (30), 19578–19585 (2021). doi:10.1021/acsomega.1c02091.
- [28] X.T. Tran, S.S. Park, S. Song, M. Haider, S. Imran, M. Hussain and H.T. Kim, *J. Mater. Sci.* **54** (4), 3156–3173 (2019). doi:10.1007/s10853-018-3043-4.
- [29] J. Li, Y. Xie, W. Lu and T.-W. Chou, *Carbon* **129**, 76–84 (2018). doi:10.1016/j.carbon.2017.11.094.
- [30] G. Xu, X. Liu, S. Huang, L. Li, X. Wei, J. Cao, L. Yang and P.K. Chu, *ACS Appl. Mater. Interfaces* **12** (1), 706–716 (2020). doi:10.1021/acsomega.9b17653.
- [31] A. Khan, A.A.P. Khan, A.M. Asiri and B.M. Abu-Zied, *Compos. Part B* **86**, 27–35 (2016). doi:10.1016/j.compositesb.2015.09.018.
- [32] S. Abazari, A. Shamsipur and H.R. Bakhsheshi-Rad, *Mater. Chem. Phys.* **301**, 127543 (2023). doi:10.1016/j.matchemphys.2023.127543.
- [33] R. Rajendran, L.K. Shrestha, K. Minami, M. Subramanian, R. Jayavel and K. Ariga, *J. Mater. Chem. A* **2** (43), 18480–18487 (2014). doi:10.1039/C4TA03996C.